Correspondence to:
S. D. Walton,
sdwalton@berkeley.edu

The Response of Electron Pitch Angle Distributions to the Upper Limit on Stably Trapped Particles

S. D. Walton[1], **I. R. Mann[2]**, **L. Olifer[2]**, **L. G. Ozeke[2]**, **C. Forsyth[3]**, **I. J. Rae[4]**, **M.-T. Walach[5]**, **K. R. Murphy[4,6]**, **S. G. Claudepierre[7]**, **H. E. Spence[8]**, and **D. N. Baker[9]**

[1]Space Sciences Laboratory, University of California, Berkeley, CA, USA, [2]Department of Physics, University of Alberta, Edmonton, AB, Canada, [3]Mullard Space Science Laboratory, University College London, Dorking, UK, [4]Department of Maths, Physics and Electrical Engineering, Northumbria University, Newcastle upon Tyne, UK, [5]Department of Physics, Lancaster University, Lancaster, UK, [6]Self, Thunder Bay, ON, Canada, [7]Department of Atmospheric and Oceanic Sciences, University of California, Los Angeles, CA, USA, [8]Institute for the Study of Earth, Oceans, and Space, University of New Hampshire, Durham, NH, USA, [9]Laboratory for Atmospheric and Space Physics, University of Colorado Boulder, Boulder, CO, USA

Abstract We use Van Allen Probes electron data during 70 geomagnetic storms to examine the response of equatorial pitch angle distributions (PADs) at $L^* = 4.0$–4.5 to a theoretical upper limit on stably trapped particle fluxes. Of the energies examined, 54 and 108 keV electron PADs isotropize to a previously assumed level within 6 hr of reaching the limit, near-identically across all 70 storms, consistent with rapid pitch angle scattering due to chorus wave interactions. In around 30% of events, 54 keV electrons completely exceed the KP limit, before being quickly subdued. 470 and 749 keV PADs show clear indications of an upper limit, though less aligned with the calculated limit used here. The consistency of an absolute upper limit shown across all events demonstrates the importance of this phenomena in both the limiting effect on electron flux and consistently influencing electron PAD evolution during geomagnetic storms. These results also highlight the need for further investigation, particularly related to the limiting of higher energy electrons.

Plain Language Summary High energy electrons in the space environment around Earth, known as the outer Van Allen radiation belt, can cause severe damage to satellites in orbit. Simultaneously measuring many electrons traveling in different directions and at different energies can help us understand which processes are present and influencing radiation belt dynamics in more detail. Our results show evidence of a process which limits electrons in the heart of the outer radiation belt to a maximum intensity level. The directional measurements provide further insight into the processes causing these energy-dependent changes, showing signs of already known mechanisms such as interaction with particular magnetic waves.

1. Introduction

Energetic (10s keV–10s MeV) electrons of Earth's outer radiation belt are highly dynamic, and important to understand due to their damaging effect on orbiting satellites (e.g., Baker et al., 2018; Wrenn, 1995). Geomagnetic activity, such as storms and substorms, are largely responsible for radiation belt dynamics (e.g., Akasofu et al., 1963; Hutchinson et al., 2011; Yokoyama, 1997), driving known enhancement, loss and transport processes such as ULF and VLF waves (e.g., Bingham et al., 2018; Horne et al., 2009; Jaynes et al., 2015; Mathie & Mann, 2000; Murphy et al., 2020; Reeves et al., 2013; Rostoker et al., 1998), and the loss of electrons via the magnetopause (e.g., Schulz & Lanzerotti, 2012; Staples et al., 2022; West et al., 1972). Scientific interest often focuses around understanding those processes in relation to the observed electron flux response.

Kennel and Petschek (1966) originally theorized that stably trapped electrons of >40 keV (integral flux) are subject to a natural upper flux limit, imposed by the generation of whistler-mode chorus waves due to pitch angle anisotropies. High levels of flux and pitch angle anisotropy will result in high levels of chorus generation. It follows therefore, that due to the ability of chorus waves to effectively scatter electron pitch angles (e.g., Horne & Thorne, 1998; Horne et al., 2003), a threshold can be reached where pitch angle scattering dominates, preventing further increases in flux. Since the original formulation, a number of studies have advanced the Kennel-Petschek framework, adapting for differential flux at higher energies (Schulz & Davidson, 1988) and incorporating relativistic effects (Mauk & Fox, 2010; Summers et al., 2009, 2011; Xiao et al., 1998). From here on, we will term this process the "Kennel-Petschek" (KP) process or limit.

More recently, observational evidence of the KP process has been presented, showing a very clear upper flux limit (Olifer et al., 2021), as well as the corresponding high amplitude chorus waves (Chakraborty et al., 2022). Studies have also shown that when reformulated in terms of differential flux, an upper limit may be present for particles at higher energies, even for >1 MeV, but would require an extremely high number of particles, rarely observed in Earth's radiation belts. A small number of studies have reported these observations, though only by specifically selecting the most extreme events available at the time (Davidson et al., 1988; Mauk & Fox, 2010; Olifer et al., 2021, 2022; Schulz & Davidson, 1988).

The KP process requires high pitch angle anisotropies and the subsequent rapid scattering of electron pitch angles. It therefore follows that the respective equatorial electron PAD should exhibit characteristic behavior during the KP process. Electron PAD's have previously been studied as useful indicators of drivers of electron flux variation and are broadly categorized into three major categories: pancake (highly isotropic, peaked at 90°), butterfly (minima at 90°, two symmetric peaks at smaller and larger pitch angles) and flattop (transitional between pancake and butterfly) (for further discussion on electron PADs, see, e.g., Gannon et al., 2007; Ozeke et al., 2022; Zhao et al., 2018, 2020).

Here, we use fitted equatorial PADs, derived from combined Van Allen Probe A and B data (Mauk et al., 2013; Spence et al., 2013) in a superposed epoch analysis (SEA), to examine their temporal evolution during the KP process at L* = 4.0–4.5, specifically during geomagnetic storms. We find that of the PADs that reach the KP level calculated from the Mauk and Fox (2010) formulation, once reached, isotropization follows, close to the level assumed in Mauk and Fox (2010) and corresponding with electron fluxes reaching a clear upper limit. Of those energies (54, 108, 470, and 749 keV), the KP effect is most pronounced at 54 and 108 keV, and less pronounced at 470 and 749 keV, though is still apparent.

2. Instrumentation and Data

Seven years (September 2012–October 2019) of Level 3 flux data from the Relativistic Electron-Proton Telescope (Baker et al., 2013) (>2 MeV) and Magnetic Electron Ion Spectrometer (MagEIS) (Blake et al., 2013) (<2 MeV) instruments aboard both Van Allen Probe A and B spacecraft are used to characterize the electron PADs. MagEIS energy channels are labeled as the modal energy from Van Allen Probe A.

To improve the quality of the analysis and achieve a continuous characterization of PADs, as explained in Chen et al. (2014), Zhao et al. (2020), and Ozeke et al. (2022), we derive equatorial pitch angles from the Van Allen Probe measurements according to the TS04D magnetic field model (Tsyganenko & Sitnov, 2005). We then fit the mapped PADs to an eighth order Legendre polynomial, from which we then derive the fluxes in 180 equally-spaced equatorial pitch angle bins between 0° and 180°. For a full description of the mapping and Legendre polynomial fitting techniques, see Ozeke et al. (2022) and Chen et al. (2014).

We use Roederer's L* parameter (Roederer, 1967) as a magnetic field reference using the TS04D magnetic field model (Tsyganenko & Sitnov, 2005). We note that while it is important to consider the dependence of L* on electron pitch angle (e.g., Tu et al., 2019; Walton et al., 2021), below L* ≲ 5.0, L* shows very little, to no dependence on pitch angle (e.g., Ozeke et al., 2022). Therefore, we calculate L* for a 90° pitch angle particle for simplicity, binning the data in 0.5 L* intervals to capture sufficient data.

To calculate the KP limit for use in this study, we use the methodology employed by Mauk and Fox (2010) as this is, to our knowledge, the most advanced framework for describing the KP process, building on the previous works of Xiao et al. (1998) and Summers et al. (2009). The Mauk and Fox (2010) calculation has also more recently become readily available computationally, published online in Mauk (2021).

Their approach defines the KP limit as the electron flux level as a function of Energy and pitch angle, at which the overall chorus wave amplitude is sustained as a result of ongoing wave growth, including amplitude losses due to wave propagation along the field line. The KP limit can be described mathematically by the condition $G \cdot R = 1$ being met, where G is the net gain of whistler mode amplitudes at the magnetic equator and R is the ionospheric reflection coefficient, typically estimated to be ~5%, which we assume in the present study. If $G \cdot R \geq 1$, wave growth can be sustained despite imperfect ionospheric wave reflection. The KP ± factor of 3 uncertainty region
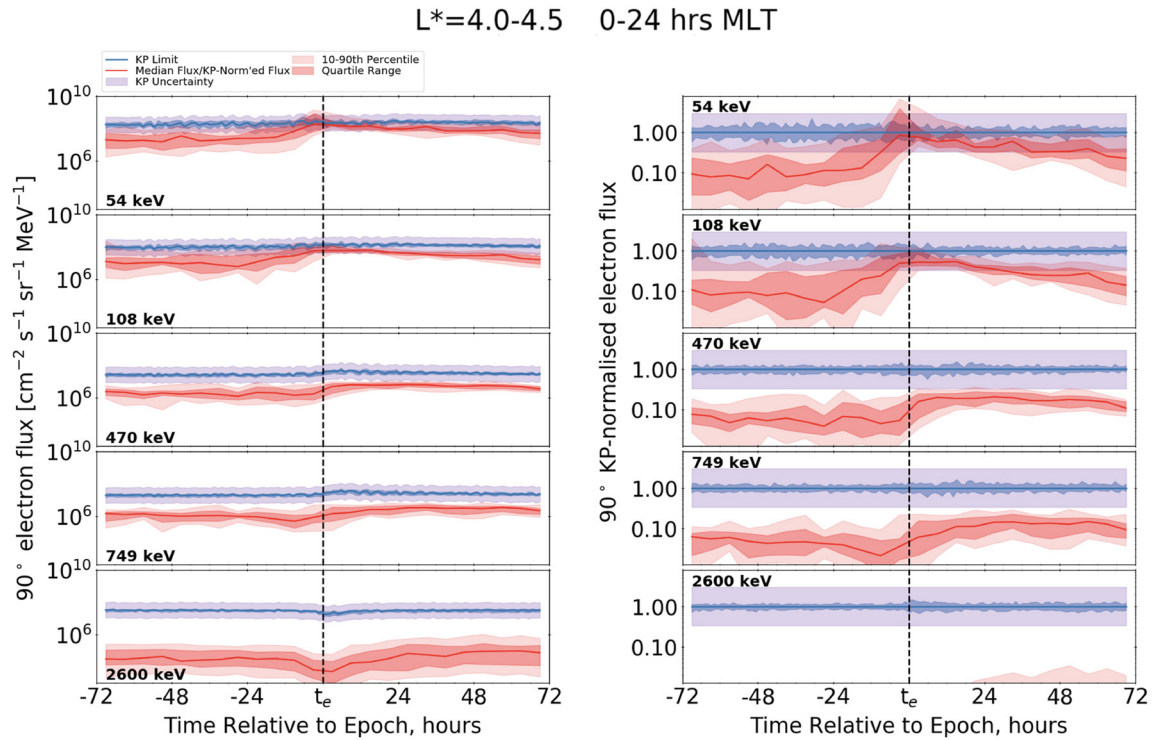
Figure 1. superposed epoch analysis for 70 storms at L* = 4.0–4.5 and the energies labeled, for an epoch at minimum Dst (vertical dashed line) ±72 hr. The left plot shows the median (red line), quartile range (darker shaded red), and 10th-90th percentile range (lighter shaded red) of 90° equatorial electron flux. The right plot is the same data as the left, but with flux normalized to the median Kennel-Petschek (KP) limit. The blue line and shaded region shows the median KP limit and its quartile range, and the purple shaded region shows the factor of 3 uncertainty in the KP limit calculation.

used in this study is directly derived from the uncertainty in the wave reflection from the ionosphere. The net gain in whistler mode amplitudes, G, is expressed in Equation 1 by:

$$LR_E\gamma(J(E,\alpha)) \approx \ln(G)V_g \tag{1}$$

Where γ is the temporal growth rate of whistler waves as a function of the current flux level, J (which, in turn, is a function of energy, E, and pitch angle, α) and V_g is the wave group speed. L and R_E represent the magnetic dipole coordinate L and Earth radii respectively. For this study, the relevant magnetic field parameters are taken from the Tsyganenko and Sitnov (2005) magnetic field model and the electron number density is taken from the Sheeley et al. (2001) empirical model. The full derivation of the final KP calculation, as well as the approximations and uncertainties that are incorporated, are extensively described in Mauk and Fox (2010) and references therein.

3. Results

In the following, we describe an SEA of the fitted electron PADs and the KP limit calculated in Mauk and Fox (2010) and as described above, at L* = 4.0–4.5, for all MLT throughout 70 Van Allen Probes era geomagnetic storms, calculating the KP limit for each individual storm before the analysis. Storms are identified using the Dst index, as described by Olifer et al. (2021) (Section 2), with all epoch times provided in their Supporting Information Table S1. The epoch time, t_e is at minimum Dst and the analysis is performed for $t_e \pm 72$ hr, with 6-hr time resolution.

3.1. Response of 90° Electron Flux

Figure 1 shows the temporal profile of the SEA for 90° fluxes. The median is plotted in red and the quartile range and 10-90th percentile range are plotted as darker and lighter shades of red, respectively. The KP limit median, quartile range and its factor of 3 uncertainty, derived from the Mauk and Fox (2010) calculation are the blue line,

blue shaded region and purple shaded region, respectively. We will collectively refer to this region as the "KP region." Figure 1 (left) shows the actual 90° flux values for 54, 108, 470, 749, and 2,600 keV, while (right) shows the 90° flux normalized to the KP limit for the same energies (KP limit = 1.00), in order to show the proximity of flux values to the KP limit on a more comparable scale between energies. In the following, we will focus on Figure 1 (right) for the KP-normalized flux unless stated otherwise.

For 54 keV electrons, the normalized 90° flux values show a large variability across ∼2 orders of magnitude pre-epoch. Median flux increases from around −12 hr to the KP limit. While the majority of 54 keV flux increases and plateaus within the KP region, approximately 25% of data exceeds the upper bound of the factor of 3 KP limit uncertainty. Within 24 hr post-epoch, 80% of data reduces below the median KP limit, concurrent with a significant reduction in data variability from ∼1.5–2 orders of magnitude pre-epoch, to <1 order of magnitude. From epoch to +72 hr, 54 keV flux gradually decreases and appears to increase in variability again with decreasing proximity to the KP limit.

108 keV results show similarly high variability to 54 keV electrons, around two orders of magnitude pre-epoch. From −12 hr to epoch, median flux increases and plateaus inside the KP region, concurrent with a significant reduction in variability, more so than 54 keV, to ≲0.5 orders of magnitude and remains constant for around 18 hr post-epoch. I.E. For 108 keV electrons, 80% of all 70 storms plateau within ≲0.5 an order of magnitude, within very close proximity to the calculated KP limit. 108 keV electron fluxes proceed to decrease in intensity (and therefore away from the KP limit) and increase in variability after ∼18 hr. The described effect in 108 keV electrons can also be observed in 470 keV electrons to a lesser degree, reducing in variability with increasing proximity to the KP limit, though the median flux remains ∼0.5 order of magnitude below the median KP limit. 749 keV electron fluxes remain entirely below the KP region and do not show any significant changes in variability, though the variability between the upper quartile and 90th percentile may reduce, and will be analyzed more closely in Section 3.3. 2,600 keV (2.6 MeV) electron fluxes typically remain far below the KP region throughout the SEA, most ≲3 orders of magnitude, and as can be seen from Figure 1 (left), do not show any significant change in variability.

In summary, for all electron energies whose fluxes plateau the KP region, the variability in fluxes decreases with proximity, as an increasing proportion of the 70 storms plateau at a similar flux intensity. For 54 keV electrons, there appears to be an 'overshoot' feature in the most extreme fluxes, before the reduction in variability. Higher energies 749 and 2,600 keV do not show any clear change in variability, particularly the 2,600 keV electron fluxes, which remain significantly below the KP region.

3.2. Response of Electron Pitch Angle Distributions

Figure 2 shows the SEA of KP-normalized, fitted electron fluxes as a function of pitch angle, for time bins selected to represent significant stages of flux limiting during storms: −66 to −60 hr (left), −6 hr to epoch (center-left) epoch to 6 hr (center), 12–18 hr (center-right) and 24–30 hr (right). These time-bins cover the pre-storm, main phase and the progression through the early recovery phase. From top to bottom, 54, 108, 470 and 749 keV electrons fluxes are shown, notably without the 2,600 keV electrons due to their lack of significance with regards to the KP limit in this particular analysis, as shown by Figure 1. The KP region is also plotted as a function of pitch angle, according to an anisotropy level of $\sin^{0.6}\alpha_{eq}$, as estimated in Mauk and Fox (2010). The colors are keyed identically to that of Figure 1.

For 54 keV electrons Figure 2 (top row), progression through the storm can be equated to that in Figure 1 when focusing on 90° flux. The "overshoot" of the KP region is clear ±6 hr of the epoch time, with there being a large, around 1.5–2 orders of magnitude spread across 80% of the events pre-epoch. Notably, from 0 to 6 hr and 12–18 hr post-epoch, while some degree of variability remains at 90°, variability is reduced to <0.5 of an order of magnitude at pitch angles ≲45° and ≳135°. The uppermost percentiles also show hints of butterfly PADs. 24–30 hr post-epoch, variability increases again as overall flux reduces in intensity and away from the KP region. 108 keV fluxes (second row) evolve similarly to 54 kev, without overshooting the KP region, but lose their 90° variability by 12 hr post-epoch, as well as at all other pitch angles.

Median 470 keV electron fluxes in Figure 2 (third row) notably do not reach the KP region, but the variability in the data still reduces significantly across all pitch angles with proximity to the KP region, from ∼1 to ∼0.5 orders
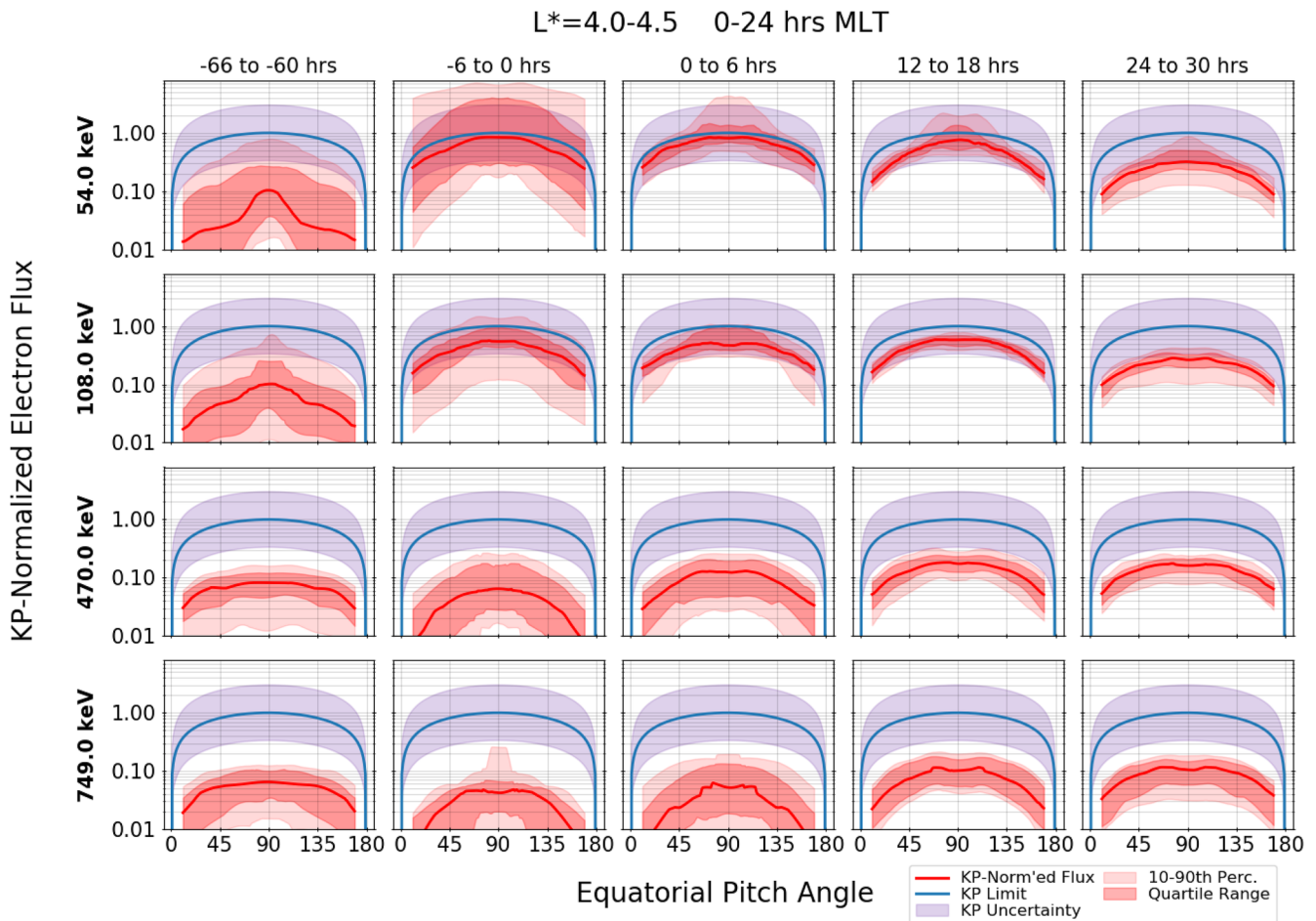
Figure 2. Superposed Epoch Analysis as in Figure 1, for (from top to bottom) 54, 108, 470 and 749 keV electrons, plotted at the selected times relative to epoch, labeled above each column. The median (red line), quartile range (darker shaded red) and 10-90th percentile range (lighter red) of electron flux normalized to the KP limit at 90° is plotted as a function of equatorial pitch angle. The median KP limit (blue line) and it's factor of 3 uncertainty (purple shaded region) are plotted as a function of equatorial pitch angle α_{eq}, according to the $\sin^{0.6}\alpha_{eq}$ level of anisotropy assumed in Mauk and Fox (2010).

of magnitude. The PAD characteristically isotropizes to around $\sin^{0.6}\alpha_{eq}$ from 12 hr onward. This effect is also observed in 759 keV electrons, though to a milder degree and with lesser proximity to the KP region.

Overall, PADs in Figure 2 appear to characteristically evolve with the proximity of 90° fluxes to the KP region. PADs across all analyzed energies typically isotropoize to $\sin^{0.6}\alpha_{eq}$ upon reaching a peak flux, and reduce in variability. This is more subtle, but still clear, with increasing energy. In the next section, we will analyze the distribution of the SEA data in more detail.

3.3. Comparison of Pitch Angle Distributions to Flux Distributions

Figure 3 shows the distribution of 90° flux values across the 70 geomagnetic storm events. The figure panel layout is identical to that of Figure 2 to allow clear reference, showing 54, 108, 470 and 749 keV electrons from top to bottom, and time bins −66 to −60 hr, −6 hr to epoch, epoch to 6 hr, 12–18 hr and 24–30 hr from left to right. The distribution of measured 90° flux values normalized to the KP limit are represented as red bars, and the 90° KP region is plotted as the vertical blue line and purple region. The median PAD for each time bin and energy is inset in the upper-left of each respective panel (shown in red), along with the KP region (blue line and purple shaded region).

The features described in Section 3.2 and shown in Figure 2 for 54 and 108 keV are emphasized in Figure 3. There is initially a relatively large spread of data pre-storm (−66 to −60 hr) in both 54 and 108 keV. For 54 keV
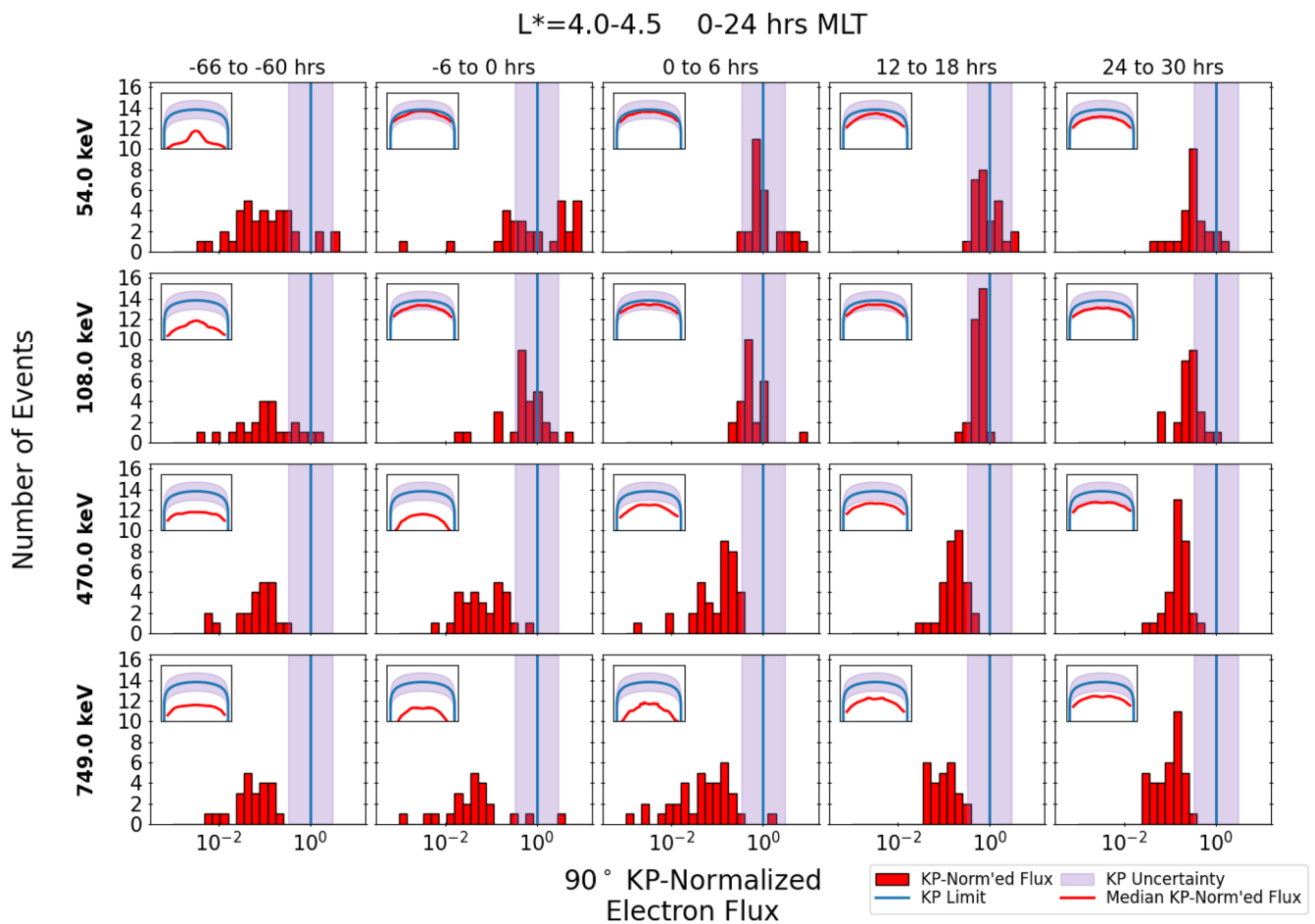
Figure 3. Superposed Epoch Analysis as in Figure 1, for (from top to bottom) 54, 108, 470 and 749 keV electrons, plotted at the selected times relative to epoch, labeled above each column. The distribution (red bars) of events is plotted as a function of electron flux normalized to the KP limit at 90°. The median KP limit is plotted as a vertical blue line, with it's factor of 3 uncertainty shaded in purple. The pitch angle distribution for each respective time, and the KP limit, is plotted in the upper-left of each panel, comparative in layout to Figure 2.

electrons, −6 hr to epoch shows somewhat bimodal distribution, with some events concentrated just under the median KP limit and a concentration of events 'overshooting' the KP region. From the epoch to +6 hr, the data becomes much more concentrated around the median KP limit and mostly within the KP region, concurrent with the PAD (upper-left of panel) closely matching the KP region anisotropy. From 12 hr onward, the spread of data increases again as many of the 70 events reduce in flux. 108 keV electron fluxes typically do not overshoot the KP region, as shown in Figures 1 and 2 and emphasized in Figure 3. As the majority of fluxes (and the respective PADs) approach the KP region, the distribution becomes increasingly modal, concentrated very close to the median KP limit by 12–18 hr after the epoch.

The 470 and 749 keV electron flux distributions from Figure 3 (bottom two rows) provide further insight into the spread of data. As the fluxes approach the KP region in both energies (from −6 hr through to 30 hr), the distributions become increasingly skewed to the right, with a leftward tail, concentrating close to the lower bound of the KP region, again, concurrent with isotropization of the PADs. This effect is, again, less pronounced for 749 keV, but clearly visible in the distribution where such an effect was not clear in the statistical PAD data alone (from Figure 2).

Overall, the flux distributions in Figure 3 informatively add to the results of Figure 2, providing a more detailed view of the spread of data. For 54 and 108 keV, the result is emphasized, showing the concentration of data within the KP region. For 470 and 749 keV, the evolution of the flux across events becomes much more clear when viewing the distributions, showing the right-skewed distribution as the fluxes approach the KP region and becoming concentrated close to the KP region during isotropization of the respective PADs.

4. Discussion

We have shown the response of fitted equatorial electron PADs to geomagnetic storms in the context of self-limitation of fluxes, specifically with regards to the theories of Kennel and Petschek (1966) and the calculation outlined in Mauk and Fox (2010). Having performed an SEA of the fitted PADs, we have presented the temporal evolution of 90° electron fluxes for ±72 hr of minimum Dst, followed by a more detailed analysis of the PAD evolution and the distribution of the 90° flux intensities across 70 geomagnetic storm events, identified as in Olifer et al. (2021). Our results show a clear evolution of different electron populations throughout the course of geomagnetic storms, highly dependent on energy.

Pre-epoch, our results demonstrate vastly differing initial flux conditions between storms, regardless of energy, followed by some form of enhancement. Higher energy electrons enhance over longer timescales than lower energies and therefore reach the KP region later in the storm, if at all. As shown in Section 3, variability in the PAD data appears to be dependent on proximity to the KP region.

54 keV electrons, being the lowest of the energies analyzed, are the first population to reach the KP region during storms, and even exceed it in ∼30% of the events analyzed, though remains highly variable in the 6 hr pre-epoch. This high flux and high variability is likely to be the result of a large number of particles in the 10s keV population being injected from the magnetotail during storm main phase (e.g., Baker et al., 1998; Jaynes et al., 2015; Murphy et al., 2018). This notion is compounded by the continuing increased flux variability around 90° throughout the recovery phase, as shown in Figure 2 (top row), compared to pitch angles closer to the loss cone. Generally, anisotropies in the 10s keV population, which we observe here, are thought to be the primary source of whistler-mode chorus waves in the outer radiation belts (e.g., Jaynes et al., 2015; Kennel & Petschek, 1966; Li et al., 2010; Sazhin & Hayakawa, 1992), which are able to effectively scatter electron pitch angles of many energies (including 54 keV) toward the atmospheric loss cone, increasing the flux at smaller pitch angles (e.g., Horne & Thorne, 1998; Horne et al., 2003). The dramatic reduction in 54 keV flux variability to mainly within the KP region observed in Figure 2 (top row), and the isotropization of the median PAD to ∼$\sin^{0.6}\alpha_{eq}$ anisotropy within 6 hr post-epoch strongly suggests that these electrons may be influenced by a self-limiting process akin to that described originally by Kennel and Petschek (1966).

Our results similarly suggest a self-limiting process for 108 keV electrons (Figure 2, second row), as they are also thought to be capable of generating chorus emissions (e.g., Jaynes et al., 2015; Li et al., 2010; Sazhin & Hayakawa, 1992, and references therein). The PAD evolution is very similar to 54 keV electrons, instead without the overwhelming quantity of injected particles required to exceed the KP region. There are mild 108 keV injection signatures within 6-hr post-epoch, where fluxes around 90° show increased variability, as well as slightly higher variability at pitch angles <45° and >125, indicating that for some events, PADs remain anisotropic. By 12–18 hr post epoch, the fluxes have, similarly to 54 keV, dramatically reduced in variability to a very small range of flux values, and isotropized to ∼$\sin^{0.6}\alpha_{eq}$.

The occurrence of a self-limiting flux process akin to that in Kennel and Petschek (1966), that is, flux limiting as a result of chorus wave generation directly by that specific energy of particles, is more difficult to conclude for our 470 and 749 keV results, not least because the authors in the mentioned study are referring to >40 keV integral electron fluxes only. As previously mentioned, later formulations of the theory (Davidson et al., 1988; Mauk & Fox, 2010; Summers et al., 2009) consider differential flux, with which, Schulz and Davidson (1988), Davidson et al. (1988), and Olifer et al. (2022) have presented observational evidence of an upper limit for electrons with energies up to 2.6 MeV. The present study uses the Mauk and Fox (2010) formulation of an upper limit, which in Figure 3 (bottom two rows) for 470 and 749 keV electron fluxes, clearly shows a relationship to right-skewed, highly modal distributions, suggesting a common upper limit observed across many different storm events. Our PAD results in Figure 2 (bottom two rows) also suggest pitch angle scattering at the upper limit, by the isotropization of the distribution. However, chorus wave generation is generally attributed to the 10–100 keV population (e.g., Sazhin & Hayakawa, 1992; Li et al., 2010; Jaynes et al., 2015, and references therein). It is clear that chorus waves are able to scatter the pitch angles of a large range of energies including >1 MeV (e.g., Bortnik & Thorne, 2007; Breneman et al., 2017; Horne & Thorne, 1998; Horne et al., 2009), so chorus waves generated by the 10–100 keV particle population cannot be ruled out as a possible contributor to the observed upper limit at higher energies. It is unclear what precise mechanism is responsible for the results in the present study and in previously mentioned studies for the flux limiting effect at energies higher than a few 100s keV.

Moreover, it appears that the modal points of Figure 2 distributions are at increasingly further from the KP limit, despite the still right-modal shapes. The 470 and 749 keV distributions peak below the entire KP region, suggesting that the Mauk and Fox (2010) calculation may be overestimating the KP limit at higher energies. As discussed above, it is unclear what may be responsible for the upper limit at higher energies, and while the KP process could still be in effect and simply overestimated, it is worth considering that another unknown process besides the KP process may be influencing this behavior. There are also multiple known processes which could enhance electron precipitation at 470 and 749 keV energies (and therefore limiting the fluxes to a lower level), such as EMIC wave scattering (e.g., Hendry et al., 2017, 2021) or ULF wave modulation of the loss cone (e.g., Brito et al., 2015; Rae et al., 2018), which are not considered by the KP limit calculation. However, it is important to emphasize that the additional known processes are not known to produce the "limiting" effect which we observe here, and so would be supplementary to some kind of flux-limiting process, KP-related or otherwise.

It is also worth noting that even though we observe a possible upper limit across all of the energies in our analysis, the enhancement mechanism is different. As mentioned, 54 and 108 keV electrons show characteristics of particle injections from the magnetotail (Figure 2) (top two rows), which is unlikely to be the case for 470 and 749 keV. Instead, 470 and 749 keV electrons and higher are thought to be either accelerated by chorus waves generated by the 10–100 keV electron 'source' population (e.g., Jaynes et al., 2015, and references therein), enhanced by ULF wave power and radial diffusion during storm recovery phase (e.g., Mann et al., 2016; Mathie & Mann, 2000; Murphy et al., 2011; Ozeke et al., 2012, 2017; Rae et al., 2012), or a combination of all of the above. Hence the observed longer timescale for the higher energies to approach the KP region. That said, regardless of the nature of enhancement and the energy dependence between populations, all energies observed in this study appear to tend toward the same fundamental behavior following that enhancement, that is, reducing in variability when approaching the region of possible influence by the KP process or at least some form of upper limiting process, and subsequent isotropization of the equatorial PAD.

5. Conclusions

We have used Legendre polynomials to fit the details of the equatorial PADs of relativistic electrons during 70 storms at L* = 4.0–4.5 and determine how they typically respond to geomagnetic storms via a SEA. The present study provides observational evidence from the Van Allen Probes mission of an upper flux limit on stably trapped electrons with 54, 108, 470 and 749 keV energies. Here, we use the Mauk and Fox (2010) formulation, based on the ideas of Kennel and Petschek (1966) as a basis for comparison with observed equatorial fluxes and PADs. We find:

1. The variability in fluxes across events for 54 and 108 keV dramatically reduces for all pitch angles upon reaching an upper limit, in strong alignment with the calculated KP limit.
2. Around 30% of events show 54 keV electron fluxes exceeding the KP region entirely, before being subdued within 6 hr to below the KP limit.
3. 470 and 749 keV 90° fluxes show reduction in variability, as well as right-skewed, highly modal distributions across all events around their peak flux, further emphasizing the presence of an upper limit, though this is appears increasingly below the KP-limit calculation with increasing energy.
4. For all energies, equatorial electron PADs evolve such that they isotropize to $\sim\sin^{0.6}\alpha_{eq}$ when close to their upper limit, suggesting the scattering of 90° pitch angles toward the loss cone.

While there is support in literature for a self-limiting, Kennel and Petschek (1966) style process at 10–100 keV energies, this is not the case for higher energies, despite the clear appearance of an upper limit in the observational data shown here and in other studies (Davidson et al., 1988; Olifer et al., 2022; Schulz & Davidson, 1988). It is open to interpretation and future work to determine the process which limits fluxes at these higher energies. Regardless of the underlying process, this is an important result for future consideration of radiation belt observations, modeling, and prediction of future dynamics.

Data Availability Statement

RBSP-ECT data are publicly available at https://rbsp-ect.newmexicoconsortium.org/science/DataDirectories.php Parameters for TS04 model are obtained from the Tsyganenko model web page (http://geo.phys.spbu.ru/~tsyganenko/modeling.html).

References

Akasofu, S.-I., Chapman, S., & Venkatesan, D. (1963). The main phase of great magnetic storms. *Journal of Geophysical Research*, *68*(11), 3345–3350. https://doi.org/10.1029/jz068i011p03345

Baker, D. N., Erickson, P. J., Fennell, J. F., Foster, J. C., Jaynes, A. N., & Verronen, P. T. (2018). Space weather effects in the Earth's radiation belts. *Space Science Reviews*, *214*(1), 17. https://doi.org/10.1007/s11214-017-0452-7

Baker, D. N., Kanekal, S. G., Hoxie, V. C., Batiste, S., Bolton, M., Li, X., et al. (2013). The Relativistic Electron-Proton Telescope (REPT) instrument on board the Radiation Belt Storm Probes (RBSP) spacecraft: Characterization of Earth's radiation belt high-energy particle populations. *Space Science Reviews*, *179*(1–4), 337–381. https://doi.org/10.1007/s11214-012-9950-9

Baker, D. N., Li, X., Blake, J. B., & Kanekal, S. (1998). Strong electron acceleration in the Earth's magnetosphere. *Advances in Space Research*, *21*(4), 609–613. https://doi.org/10.1016/S0273-1177(97)00970-8

Bingham, S. T., Mouikis, C. G., Kistler, L. M., Boyd, A. J., Paulson, K., Farrugia, C. J., et al. (2018). The outer radiation belt response to the storm time development of seed electrons and chorus wave activity during CME and CIR driven storms. *Journal of Geophysical Research: Space Physics*, *123*(12), 10139–10157. https://doi.org/10.1029/2018JA025963

Blake, J. B., Carranza, P. A., Claudepierre, S. G., Clemmons, J. H., Crain, W. R., Dotan, Y., et al. (2013). The Magnetic Electron Ion Spectrometer (MagEIS) instruments aboard the Radiation Belt Storm Probes (RBSP) spacecraft. *Space Science Reviews*, *179*(1–4), 383–421. https://doi.org/10.1007/S11214-013-9991-8/TABLES/6

Bortnik, J., & Thorne, R. (2007). The dual role of ELF/VLF chorus waves in the acceleration and precipitation of radiation belt electrons. *Journal of Atmospheric and Solar-Terrestrial Physics*, *69*(3), 378–386. https://doi.org/10.1016/J.JASTP.2006.05.030

Breneman, A. W., Crew, A., Sample, J., Klumpar, D., Johnson, A., Agapitov, O., et al. (2017). Observations directly linking relativistic electron microbursts to whistler mode chorus: Van Allen Probes and FIREBIRD II. *Geophysical Research Letters*, *44*(22), 11265–11272. https://doi.org/10.1002/2017GL075001

Brito, T., Hudson, M. K., Kress, B., Paral, J., Halford, A., Millan, R., & Usanova, M. (2015). Simulation of ULF wave-modulated radiation belt electron precipitation during the 17 March 2013 storm. *Journal of Geophysical Research: Space Physics*, *120*(5), 3444–3461. https://doi.org/10.1002/2014JA020838

Chakraborty, S., Mann, I. R., Watt, C. E., Rae, I. J., Olifer, L., Ozeke, L. G., et al. (2022). Intense chorus waves are the cause of flux-limiting in the heart of the outer radiation belt. *Scientific Reports*, *12*(1), 1–13. https://doi.org/10.1038/s41598-022-26189-9

Chen, Y., Friedel, R. H. W., Henderson, M. G., Claudepierre, S. G., Morley, S. K., & Spence, H. E. (2014). REPAD: An empirical model of pitch angle distributions for energetic electrons in the Earth's outer radiation belt. *Journal of Geophysical Research: Space Physics*, *119*(3), 1693–1708. https://doi.org/10.1002/2013JA019431

Davidson, G. T., Filbert, P. C., Nightingale, R. W., Imhof, W. L., Reagan, J. B., & Whipple, E. C. (1988). Observations of intense trapped electron fluxes at synchronous altitudes. *Journal of Geophysical Research*, *93*(A1), 77–95. https://doi.org/10.1029/ja093ia01p00077

Gannon, J. L., Li, X., & Heynderickx, D. (2007). Pitch angle distribution analysis of radiation belt electrons based on Combined Release and Radiation Effects Satellite Medium Electrons A data. *Journal of Geophysical Research*, *112*(A5), 5212. https://doi.org/10.1029/2005JA011565

Hendry, A. T., Rodger, C. J., & Clilverd, M. A. (2017). Evidence of sub-MeV EMIC-driven electron precipitation. *Geophysical Research Letters*, *44*(3), 1210–1218. https://doi.org/10.1002/2016GL071807

Hendry, A. T., Rodger, C. J., Clilverd, M. A., & Morley, S. K. (2021). Evidence of sub-MeV EMIC-driven trapped electron flux dropouts from GPS observations. *Geophysical Research Letters*, *48*(9), e2021GL092664. https://doi.org/10.1029/2021GL092664

Horne, R. B., Glauert, S. A., & Thorne, R. M. (2003). Resonant diffusion of radiation belt electrons by whistler-mode chorus. *Geophysical Research Letters*, *30*(9), 1493. https://doi.org/10.1029/2003GL016963

Horne, R. B., Lam, M. M., & Green, J. C. (2009). Energetic electron precipitation from the outer radiation belt during geomagnetic storms. *Geophysical Research Letters*, *36*(19), L19104. https://doi.org/10.1029/2009GL040236

Horne, R. B., & Thorne, R. M. (1998). Potential waves for relativistic electron scattering and stochastic acceleration during magnetic storms. *Geophysical Research Letters*, *25*(15), 3011–3014. https://doi.org/10.1029/98GL01002

Hutchinson, J. A., Wright, D. M., & Milan, S. E. (2011). Geomagnetic storms over the last solar cycle: A superposed epoch analysis. *Journal of Geophysical Research*, *116*(A9), A09211. https://doi.org/10.1029/2011JA016463

Jaynes, A. N., Baker, D. N., Singer, H. J., Rodriguez, J. V., Loto'aniu, T. M., Ali, A. F., et al. (2015). Source and seed populations for relativistic electrons: Their roles in radiation belt changes. *Journal of Geophysical Research: Space Physics*, *120*(9), 7240–7254. https://doi.org/10.1002/2015JA021234

Kennel, C. F., & Petschek, H. E. (1966). Limit on stably trapped particle fluxes. *Journal of Geophysical Research*, *71*(1), 1–28. https://doi.org/10.1029/JZ071i001p00001

Li, W., Thorne, R. M., Nishimura, Y., Bortnik, J., Angelopoulos, V., McFadden, J. P., et al. (2010). THEMIS analysis of observed equatorial electron distributions responsible for the chorus excitation. *Journal of Geophysical Research*, *115*(A6), A00F11. https://doi.org/10.1029/2009JA014845

Mann, I. R., Ozeke, L. G., Murphy, K. R., Claudepierre, S. G., Turner, D. L., Baker, D. N., et al. (2016). Explaining the dynamics of the ultra-relativistic third Van Allen radiation belt. *Nature Physics*, *12*(10), 978–983. https://doi.org/10.1038/nphys3799

Mathie, R. A., & Mann, I. R. (2000). A correlation between extended intervals of ULF wave power and storm-time geosynchronous relativistic electron flux enhancements. *Geophysical Research Letters*, *27*(20), 3261–3264. https://doi.org/10.1029/2000GL003822

Mauk, B. H. (2021). Software for "radiation belts of the solar system". *Zenodo*. https://doi.org/10.5281/zenodo.4782323

Mauk, B. H., & Fox, N. J. (2010). Electron radiation belts of the solar system. *Journal of Geophysical Research*, *115*(A12), 12220. https://doi.org/10.1029/2010JA015660

Mauk, B. H., Fox, N. J., Kanekal, S. G., Kessel, R. L., Sibeck, D. G., & Ukhorskiy, A. (2013). Science objectives and rationale for the radiation belt storm probes mission. *Space Science Reviews*, *179*(1–4), 3–27. https://doi.org/10.1007/S11214-012-9908-Y/FIGURES/23

Murphy, K. R., Mann, I. R., Sibeck, D. G., Rae, I. J., Watt, C., Ozeke, L. G., et al. (2020). A framework for understanding and quantifying the loss and acceleration of relativistic electrons in the outer radiation belt during geomagnetic storms. *Space Weather*, *18*(5), e2020SW002477. https://doi.org/10.1029/2020SW002477

Murphy, K. R., Rae, I. J., Mann, I. R., & Milling, D. K. (2011). On the nature of ULF wave power during nightside auroral activations and substorms: 1. Spatial distribution. *Journal of Geophysical Research*, *116*(A5), A00I22. https://doi.org/10.1029/2010JA015757

Murphy, K. R., Watt, C. E. J., Mann, I. R., Rae, I. J., Sibeck, D. G., Boyd, A. J., et al. (2018). The global statistical response of the outer radiation belt during geomagnetic storms. *Geophysical Research Letters*, *45*(9), 3783–3792. https://doi.org/10.1002/2017GL076674

Olifer, L., Mann, I. R., Claudepierre, S. G., Baker, D. N., Spence, H. E., & Ozeke, L. G. (2022). A natural limit to the spectral hardness of worst case electron radiation in the terrestrial Van Allen belt. *Journal of Geophysical Research: Space Physics*, *127*(8), e2022JA030506. https://doi.org/10.1029/2022JA030506

Olifer, L., Mann, I. R., Kale, A., Mauk, B. H., Claudepierre, S. G., Baker, D. N., et al. (2021). A tale of two radiation belts: The energy-dependence of self-limiting electron space radiation. *Geophysical Research Letters*, *48*(20), e2021GL095779. https://doi.org/10.1029/2021GL095779

Ozeke, L. G., Mann, I. R., Murphy, K. R., Rae, I. J., Milling, D. K., Elkington, S. R., et al. (2012). ULF wave derived radiation belt radial diffusion coefficients. *Journal of Geophysical Research*, *117*(A4), A04222. https://doi.org/10.1029/2011JA017463

Ozeke, L. G., Mann, I. R., Murphy, K. R., Sibeck, D. G., & Baker, D. N. (2017). Ultra-relativistic radiation belt extinction and ULF wave radial diffusion: Modeling the September 2014 extended dropout event. *Geophysical Research Letters*, *44*(6), 2624–2633. https://doi.org/10.1002/2017GL072811

Ozeke, L. G., Mann, I. R., Olifer, L., Claudepierre, S. G., Spence, H. E., & Baker, D. N. (2022). Statistical characteristics of energetic electron pitch angle distributions in the Van Allen Probe era: 1. Butterfly distributions with flux peaks at preferred pitch angles. *Journal of Geophysical Research: Space Physics*, *127*(3), e2021JA029907. https://doi.org/10.1029/2021JA029907

Rae, I. J., Mann, I. R., Murphy, K. R., Ozeke, L. G., Milling, D. K., Chan, A. A., et al. (2012). Ground-based magnetometer determination of in situ Pc4–5 ULF electric field wave spectra as a function of solar wind speed. *Journal of Geophysical Research*, *117*(A4), 4221. https://doi.org/10.1029/2011JA017335

Rae, I. J., Murphy, K. R., Watt, C. E. J., Halford, A. J., Mann, I. R., Ozeke, L. G., et al. (2018). The role of localized compressional ultra-low frequency waves in energetic electron precipitation. *Journal of Geophysical Research: Space Physics*, *123*(3), 1900–1914. https://doi.org/10.1002/2017JA024674

Reeves, G. D., Spence, H. E., Henderson, M. G., Morley, S. K., Friedel, R. H., Funsten, H. O., et al. (2013). Electron acceleration in the heart of the Van Allen radiation belts. *Science*, *341*(6149), 991–994. https://doi.org/10.1126/science.1237743

Roederer, J. G. (1967). On the adiabatic motion of energetic particles in a model magnetosphere. *Journal of Geophysical Research*, *72*(3), 981–992. https://doi.org/10.1029/JZ072i003p00981

Rostoker, G., Skone, S., & Baker, D. N. (1998). On the origin of relativistic electrons in the magnetosphere associated with some geomagnetic storms. *Geophysical Research Letters*, *25*(19), 3701–3704. https://doi.org/10.1029/98GL02801

Sazhin, S., & Hayakawa, M. (1992). Magnetospheric chorus emissions: A review. *Planetary and Space Science*, *40*(5), 681–697. https://doi.org/10.1016/0032-0633(92)90009-D

Schulz, M., & Davidson, G. T. (1988). Limiting energy spectrum of a saturated radiation belt. *Journal of Geophysical Research*, *93*(A1), 59–76. https://doi.org/10.1029/ja093ia01p00059

Schulz, M., & Lanzerotti, L. J. (2012). *Particle diffusion in the radiation belts* (Vol. 7). Springer Science & Business Media.

Sheeley, B. W., Moldwin, M. B., Rassoul, H. K., & Anderson, R. R. (2001). An empirical plasmasphere and trough density model: CRRES observations. *Journal of Geophysical Research*, *106*(A11), 25631–25641. https://doi.org/10.1029/2000JA000286

Spence, H. E., Reeves, G. D., Baker, D. N., Blake, J. B., Bolton, M., Bourdarie, S., et al. (2013). Science goals and overview of the radiation belt storm probes (RBSP) energetic particle, composition, and thermal plasma (ECT) suite on NASA's Van Allen Probes mission. *Space Science Reviews*, *179*(1–4), 311–336. https://doi.org/10.1007/s11214-013-0007-5

Staples, F. A., Kellerman, A., Murphy, K. R., Rae, I. J., Sandhu, J. K., & Forsyth, C. (2022). Resolving magnetopause shadowing using multi-mission measurements of phase space density. *Journal of Geophysical Research: Space Physics*, *127*(2), e2021JA029298. https://doi.org/10.1029/2021JA029298

Summers, D., Tang, R., & Omura, Y. (2011). Effects of nonlinear wave growth on extreme radiation belt electron fluxes. *Journal of Geophysical Research*, *116*(A10), 10226. https://doi.org/10.1029/2011JA016602

Summers, D., Tang, R., & Thorne, R. M. (2009). Limit on stably trapped particle fluxes in planetary magnetospheres. *Journal of Geophysical Research*, *114*(A10), 10210. https://doi.org/10.1029/2009JA014428

Tsyganenko, N. A., & Sitnov, M. I. (2005). Modeling the dynamics of the inner magnetosphere during strong geomagnetic storms. *Journal of Geophysical Research*, *110*(A3), A03208. https://doi.org/10.1029/2004JA010798

Tu, W., Xiang, Z., & Morley, S. K. (2019). Modeling the magnetopause shadowing loss during the June 2015 dropout event. *Geophysical Research Letters*, *46*(16), 9388–9396. https://doi.org/10.1029/2019GL084419

Walton, S. D., Forsyth, C., Rae, I. J., Watt, C. E. J., Thompson, R. L., Horne, R. B., et al. (2021). Cross-L* coherence of the outer radiation belt during storms and the role of the plasmapause. *Journal of Geophysical Research: Space Physics*, *126*(10), e2021JA029308. https://doi.org/10.1029/2021JA029308

West, H. I., Buck, R. M., & Walton, J. R. (1972). Shadowing of electron azimuthal-drift motions near the noon magnetopause. *Nature Physical Science*, *240*(97), 6–7. https://doi.org/10.1038/physci240006a0

Wrenn, G. L. (1995). Conclusive evidence for internal dielectric charging anomalies on geosynchronous communications spacecraft. *Journal of Spacecraft and Rockets*, *32*(3), 514–520. https://doi.org/10.2514/3.26645

Xiao, F., Thorne, R. M., & Summers, D. (1998). Instability of electromagnetic R-mode waves in a relativistic plasma. *Physics of Plasmas*, *5*(7), 2489–2497. https://doi.org/10.1063/1.872932

Yokoyama, N., & Kamide, Y. (1997). Statistical nature of geomagnetic storms. *Journal of Geophysical Research: Space Physics*, *102*(A7), 14215–14222. https://doi.org/10.1029/97JA00903

Zhao, H., Friedel, R. H. W., Chen, Y., Baker, D. N., Li, X., Malaspina, D. M., et al. (2020). Equatorial pitch angle distributions of 1–50 keV electrons in Earth's inner magnetosphere: An empirical model based on the Van Allen Probes observations. *Journal of Geophysical Research: Space Physics*, *126*(1), e2020JA028322. https://doi.org/10.1029/2020JA028322

Zhao, H., Friedel, R. H. W., Chen, Y., Reeves, G. D., Baker, D. N., Li, X., et al. (2018). An empirical model of radiation belt electron pitch angle distributions based on Van Allen Probes measurements. *Journal of Geophysical Research: Space Physics*, *123*(5), 3493–3511. https://doi.org/10.1029/2018JA025277